Results in Engineering 26 (2025) 104727

Contents lists available at ScienceDirect

Results in Engineering

journal homepage: www.sciencedirect.com/journal/results-in-engineering

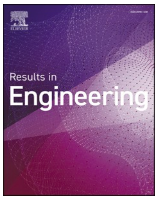

Research paper

MPC based frequency control of an autonomous microgrid integrated with electric vehicles

Abdullahi Bala Kunya [a,b,*], Muhamad M. Mundu [a], Aminu Babangida [c], Péter Tamás Szemes [c]

[a] *Department of Electrical, Telecommunications and Computer Engineering, Kampala International University, Western Campus, Ishaka, Uganda*
[b] *Department of Electrical Engineering, Ahmadu Bello University, Zaria, Nigeria*
[c] *Department of Vehicles Engineering, Vehicles and Mechatronics Institute, Faculty of Engineering, University of Debrecen, Ótemető u. 2-4, Debrecen 4028, Hungary*

ARTICLE INFO

Keywords:
Autonomous microgrid;Electric vehicle aggregator;Energy storage system;Fuel cell
Load frequency control
Model predictive control

ABSTRACT

Although electric vehicles (EVs) offer bidirectional charging and can serve as mobile energy storage units, integrating them into microgrids and enabling them to participate in load frequency control (LFC) has proven to be a significant challenge. One of the crucial issues is the unpredictability of EV usage patterns, which can lead to sudden fluctuations in generation-demand balance. This unpredictability makes it difficult to coordinate EV charging and discharging with the grid's frequency control needs. Classical control techniques lack the capability to handle the EV's stochastic behavior. To address this, the study proposes the integration of a battery energy storage system to maintain continuous generation – demand balance. Then, a finite horizon model predictive control (MPC) is applied for the LFC of a two-area islanded MG integrated with the EV charging station. The MPC generates the optimal signals for the optimal adjustment of the power generation of the dispatchable sources as well as the EV aggregators. To evaluate system stability, the local input-to-state stability (ISS) criterion is employed. Simulation results demonstrate that the proposed MPC-based LFC outperforms conventional methods in terms of frequency nadir, settling time, and rate of change of frequency (RoCoF). Under a 2 % step load perturbation in one of the control areas (CAs), the proposed MPC reduces frequency nadir to −0.0306 Hz (a 12.9 % improvement over the best alternative), limits RoCoF to −0.0524 Hz/s (a 17.4 % enhancement), and achieves a minimum steady-state frequency deviation of 4.14 × 10^{-3} Hz (a 1.9 % reduction). Furthermore, in response to random load fluctuations and renewable energy source (RES) variability, the proposed controller ensures that frequency deviations remain within ±0.02 Hz, while RoCoF is constrained within ±0.02 Hz/s, demonstrating superior robustness, constraint handling and faster convergence.

Nomenclature

P_i^{tie}	*i*th CA tie-power
f_i	*i*th CA frequency
ACE_i	*i*th CA area control error
ϕ_i	frequency bias constant of *i*th CA
γ_{12}	ratio of CA 1 to CA 2 rated capacities
$\boldsymbol{P_{DEG}}$	diesel engine generator output power
$\boldsymbol{P_{PV}}$	output power of PV system
$\boldsymbol{P_{EV}}$	scheduled power of EV fleet
P_{FC}	fuel cell output power
$\boldsymbol{P_i^D}$	load (as disturbance) in *i*th CA
$\boldsymbol{K_{pi}}$	gain of *i*th CA
K_{EV}	gain of EV system
T_{pi}	*i*th CA time constant
T_{PV}	PV time constant
T_{BES}	BES time constant
T_{EV}	EV time constant
T_{DEG}	DEG time constant
T_{FC}	FC time constant
$T^0_{(1,\ 2)}$	synchroizing coeffcient
T_s	sampling time
Ψ	vector of the control variables
$\bar{y}$	predicted output
u_0	initial control input
$\mathscr{k}$	sampling time
$\bar{u}$	predicted control input
x	vector of state variables
$\mathbb{Z}^+$	set of postive integers
$\mathbb{R}$	set of real numbers
y_{ℓ}	controlled output,

(*continued on next page*)

---

[*] Corresponding author.
E-mail address: abkunya@kiu.ac.ug (A.B. Kunya).

https://doi.org/10.1016/j.rineng.2025.104727
Received 4 January 2025; Received in revised form 9 February 2025; Accepted 26 March 2025
Available online 27 March 2025

(*continued*)

$y_{\mathscr{k}}$	constrained output
A_{ζ}, B_{ζ}, $\mathscr{F}_{\zeta}$	state matrices
u_{min}, u_{max}	limits of the control input
y_{min}, y_{max}	limits of the constrained output
ACE_{ref}	reference area control error
μ	ACE weighting matrix
ξ	control variables weighting matrix
Δf_i^{min}, Δf_i^{max}	limits of fequency deviation
ψ_{DEG}	DEG optimal control signal
ψ_{FC}	FC optimal control signal
ψ_{EV}	EV optimal control signal
n_d	number of disturbances
n_{ℓ}	number of controlled output
$n_{\mathscr{k}}$	number of constrained output

1. Introduction

Frequency control in autonomous micro-grids (MGs) is generally challenging. This is largely due to the lack of inertial support from the main grid, leading to the low inertia with drastic rate of change of frequency (RoCoF) and large frequency nadir as possible consequences [1]. In addition, frequency fluctuation (an indicator of mismatch between power generation and consumption) is often attributed to the intermittent nature of the renewable energy sources (RES) [2,3]. To reduce the adverse damping effects of non-inertial RES in islanded MG, especially while handling sudden load variations, large scale energy storage systems (ESS) such as battery, super and ultra-capacitors, flywheel or superconducting magnetic energy systems are utilized. Some of these systems like flywheel ESS are quite sluggish and therefore not suitable for arresting frequency instability [4,5]. While the battery ESS (BESS) is known to be cost-ineffective amounting to about 40 % of the total installation cost of the MG [6,7]. Therefore, ESS of EV is seen as a promising alternative for frequency stability. This is mainly due to the fast charging/discharging of EV and the robust algorithms embedded in their aggregators. It has been established that EVs participation in the LFC is cheaper than BESS [8,9].

Nevertheless, there are number of issues associated with engaging EV to participate in LFC. Uncertainties in the EV aggregator to EVs' stochastic behavior [5,10], delay due to communication between the LFC controller and the aggregator [11,12], frequent charging and discharging which is at the detriment to the lifespan of EV's ESS [13], are among the identified issues [14,15]. Moreover, the controller design requirements such as accuracy, robustness, and simplicity in the implementation are of great concern when EVs are made to participate in LFC [14,16]. As such, numerous research works proposed various techniques to address these problems.

Thus, the studies in [8,17] assessed the uncertainty in the available dispatch capacity and time delay associated with charging control of the EVs and their impact on LFC. The EVs were made to take part in a multi-objective, H_2/H_∞-based LFC. Other similar studies combined two controllers in order to achieve better performance [18,19]. In spite of the improvement in the stability, it is inefficient hybridizing two controllers to perform a task accomplishable by only one. Moreover, with multiple controllers, it is difficult to effectively incorporate some constraints such as the frequency fluctuation limits, ramp-rates or RoCoF limits [20]. Stability of MG with EV is investigated in [11,21]. With aid of the solution of Linear Matrix Inequalities (LMI) formed using Lyapunov Krasovskii (LK) function, maximum allowable time delay for the MG stability is obtained. However, forming the LMI using LK is computationally complex and as such it will be difficult to implement. In [22], a Fractional-order PID (FOPID) controller optimized using Sine Cosine Algorithm, is applied for LFC in a 2-area system incorporated with EVs. In a similar studies with the FOPID tuned with particle swarm (PSO) and aquila optimizer (AO) are presented in [17] and [23] respectively. Impact of delay in the wireless communicates between the EV and the controller is also examined [24]. However, in most of similar studies, wide stability delay margins are observed and is largely due to the EV charging pattern and demand response control incorporated. Effects of EV participation in secondary frequency modulation based on area control error (ACE) is analyzed in [25,26].

Other ancillary services are combined with the LFC to achieved better responses [27,28]. In [27], a hybrid of ANFIS and ANN are used to control the energy flows and frequencies of two-area MG with EV. In [28], LFC and AVR loops synchronized by introducing a slow optimal control action on the AVR loop to improve the LFC.

Moreover, there are studies that employed model predictive control (MPC) for LFC and ascertain the participation of EV in the LFC of conventional PS grid-connected or islanded MG [29,30]. For instance, in [31], plug-in EV (PEV) is employed for frequency control in a standalone smart power system power through a diesel engine generator (DEG) and photovoltaic (PV) systems. The load fluctuations and system uncertainties handled by an active MPC. As such, a state observer is required to estimate the unmeasurable states. Similar control scheme is used in [32] to carryout LFC in an islanded AC MG supplied from wind turbine (WT), PV and PEV. The MPC is designed to forecast the future control action following a sinusoidal load disturbance. In [33], a tube-based MPC is proposed to provide control signals to improve the dynamic response of aggregated EVs to LFC of RES-penetrated islanded PS. A reduced order model is obtained by lumping the variations in the load, WT, PV and the aggregated EVs. Uncertainties brought by external disturbances are matched using the charging/discharging of aggregated EVs. The impact of the communication delay is also investigated by conducting a stability analysis to obtain the delay margin. Likewise, an MPC-based LFC for MG with EV is presented in [34,9]. The optimal design of the MPC is constrained by generation rate of the DEGs, frequency fluctuations, among others. The ESS of EVs are designed to compensate frequency fluctuations in [35]. A centralized and decentralized MPC is optimally designed to control EVs and WTs participating in the LFC. Also, [36] proposed the use of MPC for the EV aggregators participating in LFC. EV users' convenience and payment from the utility are incorporated in the constraints while designing the MPC. Conversely, in all these reviewed MPC-based LFC studies, all the state variables were assumed to be accessible to the MPC. This assumption is far from reality, since not all the states are not measurable [29,37]. In addition, most of the study designed the LFC with decentralized control architecture. One major disadvantage of decentralized control is the potential lack of coordination between subsystems, which can lead to suboptimal performance or instability in the overall system [30]. Since each controller operates independently with limited communication, it may fail to account for the interdependencies between different CAs. This can result excessive oscillations and imbalances in the tie-line power exchanges. Hence, this proposed study proposed robust MPC controller with centralized architecture for the LFC in a two-area MG with EV. Instead of optimizing the entire time horizon as applicable to most optimal controller such as LQR, the proposed MPC optimizes in a receding time window. The unique contributions that can be credited to this study include;

- Improving the performance of LFC of a two-area MG taking into consideration the stochastic behaviour of the EVs and the fluctuations of renewable energy sources,
- Applying a robust finite horizon MPC controller due its predictive capability to generate the future behavior of the EV aggregator and generate control actions in advance. The LFC is designed with centralized control architecture to ensure that both CAs are controlled simultaneously.
- Constraining the RoCoF of the two areas along with other typical LFC constraints, using a finite horizon MPC used as the supplementary controller.

The remaining part of the paper is organized with the MG modelling and frequency controller design presented in Section II and III respectively. In addition, the simulation results are comprehensively discussed in Section IV, and the paper is concluded in Section V.

2. Microgrid modelling

Micro grid (MG) is formed by cluster of ESS, renewable and non-renewable micro-sources such as WT, PV, DEG, fuel cell (FC) and loads [10]. In modern day MG, fleet of EVs through the aggregator is often integrated to the MG and are made to provide ancillary services.

In this study, an islanded MG with two control areas supplied from various micro-sources is proposed. The first control area (CA_1) is powered from PV and DEG systems and integrated with a fleet of EVs. The EV aggregator serves as an interface between the EV charging stations (CSs) and the MG. The second control area (CA_2) is equipped with a WT, FC and battery energy storage (BES).

2.1. Tie-power modelling

The model for the tie-power change in CA_1, ΔP_1^{tie} can be derived in *s*-domain as function of deviations of area frequencies, as shown in (1),

$$\Delta P_1^{tie} = \frac{2\pi T^0_{(1,\ 2)}}{s}[\Delta F_1\ (s) - \Delta F_2(s)];\ \Delta P_2^{tie} = -\gamma_{12}\ \Delta P_1^{tie} \tag{1}$$

Where γ_{12} is the ratio of the rated capacities of CA_1 and CA_2. In this paper, the CAs are identical, therefore γ_{12} is unity.

2.2. EV modelling

Depending on the mode of the operation of the EVs, the direction of the power flow can be grid-to-vehicle (charging mode) or vehicle-to-grid (discharging) mode [38]. Due to the stochastic nature of the charging pattern, an EV can be disconnected at any time during the charging/-discharging period. This is undesirable to the frequency response. The frequency change due to this scenario, is constrained to a band of f_{EV}^{min} and f_{EV}^{max}. In addition, the proposed scheme constrained the upper and lower limits of the charging/ discharging power of the EV, P_{EV}^{min} and P_{EV}^{max} respectively.

Fig. 1 shows the droop characteristic (P - *f*) of EV charging. P_{ref} is the reference charging power where the MG frequency stabilizes. The EV is set to discharges for frequency, f: $f_{EV}^{min} \le f \le f_0$. For frequency, $f < f_{EV}^{min}$, the EV reaches it discharge limit, P_{EV}^{min}. This is achieved with aid of a saturation function, as shown in (2). With the droop characteristics, the dynamics of the EV is modelled as shown in Fig. 2.

$$\Delta P_{EV}(s) = \frac{1}{1+sT_{EV}}\left(\psi_{EV}(s) - K_{EV} sat_{f_{EV}^{min}}^{f_{EV}^{max}}\left\{\frac{\Delta F_1(s)}{R_{EV}}\right\}\right) \tag{2}$$

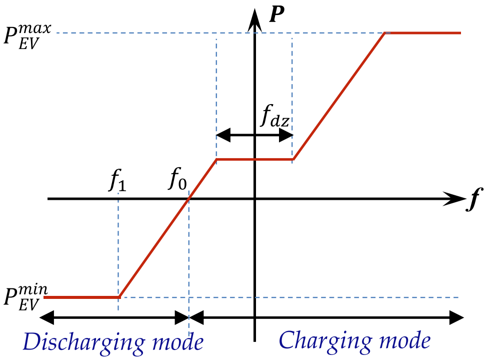

Fig. 1. EV charging $P - f$ characteristics.

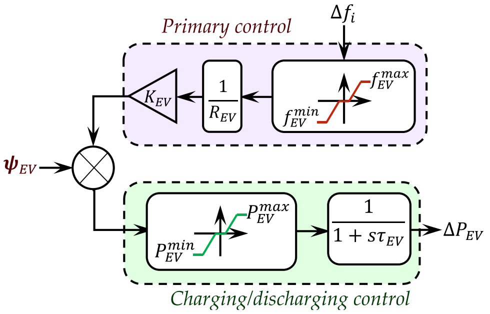

Fig. 2. EV primary control and charging model.

2.3. Frequency deviation modelling

The frequency deviation, ΔF_1 for CA_1 is modelled as first order transfer function of the generation-demand mismatches,

$$\Delta F_1(s) = \frac{K_{p1}}{1+sT_{p1}}\begin{bmatrix} P_{DEG}(s) + P_{PV}(s) + \\ P_{EV}(s) - P_1^D(s) - P_1^{tie} \end{bmatrix} \tag{3}$$

Similarly, ΔF_2 also obtained as,

$$\Delta F_2(s) = \frac{K_{p2}}{1+sT_{p2}}\begin{bmatrix} P_{FC}(s) + P_{WT}(s) + \\ P_{BES}(s) - P_2^D(s) - P_2^{tie} \end{bmatrix} \tag{4}$$

Where P_1^D and $P_2^D$are the load disturbances in CA_1 and CA_2 respectively, which are primarily the source of the system perturbation. A simplified transfer function model of the MG system is depicted in Fig. 3.

2.4. Micro-sources modelling

Although some of the micro-sources in the MG exhibit higher-order dynamics, such as the FC, this study employs approximate first-order models. With this approximation, the essential dynamics of the micro-sources are captured devoid the complexity of higher-order representations. The WT, PV and DEGs powers are modelled as in (5) – (7),

$$\Delta P_{PV}(s) = \frac{1}{1+sT_{PV}}\Delta\Omega_{PV}(s) \tag{5}$$

$$\Delta P_{WT}(s) = \frac{1}{1+sT_{WT}}\Delta\Omega_{WT}(s) \tag{6}$$

$$\Delta P_{DEG}(s) = \frac{1}{1+sT_{DEG}}\left(\psi_{DEG}(s) - \frac{\Delta F_1(s)}{R_1}\right) \tag{7}$$

Besides its high-order dynamics, the FC model is also characterized by some form of nonlinearities. However, since power system control studies concentrates on low-frequency domain, the impact of the nonlinearity is insignificant. Therefore, the FC's transfer functions are simplified to first-order lag models as shown in (8);

$$\Delta P_{FC}(s) = \frac{1}{1+sT_{FC}}\left(\psi_{FC}(s) - \frac{\Delta F_2(s)}{R_2}\right) \tag{8}$$

The complete transfer function model of the 2-CA MG is shown in Fig. 3.

The output of the system is the area control error, *ACE* formed by combining the frequency deviation of each CA and that of the tie-line power. It is, thus, formulated as in (9);

$$ACE_i = \phi_i \Delta f_i + \Delta P_i^{tie}; i = 1,\ 2 \tag{9}$$

Where ϕ_i is the frequency bias constants of *i*th CA. Rearranging the modelling equations in matrix form, the state space model of the 2-area MG is formulated as in (10) and (11).

$$\begin{pmatrix} \Delta\dot{f}_1 \\ \Delta\dot{f}_2 \\ \dot{P}_{DEG} \\ \dot{P}_{EV} \\ \dot{P}_{FC} \\ \Delta\dot{P}_1^{tie} \end{pmatrix} = \begin{pmatrix} -\frac{K_{p1}}{\tau_{p1}} & 0 & -\frac{1}{\tau_{p1}} & 0 & \frac{K_{EV}}{\tau_{EV}} & 0 \\ 0 & -\frac{\tau_{BES}K_{p2}+1}{\tau_{p2}\tau_{BES}} & 0 & 0 & 1 & -\frac{\gamma_{12}K_{p2}}{\tau_{p2}} \\ -\frac{1}{R_1\tau_{DEG}} & 0 & -\frac{1}{R_1\tau_{DEG}} & 0 & 0 & 0 \\ \frac{K_{EV}}{\tau_{EV}} & 0 & 0 & -\frac{K_{EV}}{\tau_{EV}} & 0 & 0 \\ 0 & \frac{1}{R_2\tau_{FC}} & 0 & 0 & -\frac{1}{R_2\tau_{FC}} & 0 \\ 2\pi T^0_{(1,\ 2)} & -2\pi\gamma_{12}T^0_{(1,\ 2)} & 0 & 0 & 0 & 0 \end{pmatrix} \begin{pmatrix} \Delta f_1 \\ \Delta f_2 \\ P_{DEG} \\ P_{EV} \\ P_{FC} \\ \Delta P_1^{tie} \end{pmatrix}$$

$$+ \begin{pmatrix} 0 & 0 & 0 \\ 0 & 0 & 0 \\ \frac{1}{\tau_{DEG}} & 0 & 0 \\ 0 & \frac{K_{EV}}{\tau_{EV}} & 0 \\ 0 & 0 & \frac{1}{\tau_{FC}} \\ 0 & 0 & 0 \end{pmatrix} \begin{pmatrix} \psi_{DEG} \\ \psi_{EV} \\ \psi_{FC} \end{pmatrix}^T + \begin{pmatrix} -\frac{K_{p1}}{T_{p1}} & 0 \\ 0 & -\frac{K_{p2}}{T_{p2}} \\ 0 & 0 \\ 0 & 0 \\ 0 & 0 \\ 0 & 0 \end{pmatrix} \begin{pmatrix} P_1^D \\ P_2^D \end{pmatrix}^T$$

$$+ \begin{pmatrix} -\frac{1}{\tau_{PV}} & 0 \\ 0 & -\frac{1}{\tau_{WT}} \\ 0 & 0 \\ 0 & 0 \\ 0 & 0 \\ 0 & 0 \end{pmatrix} \begin{pmatrix} \psi_{PV} \\ \psi_{WT} \end{pmatrix}^T \tag{10}$$

$$\begin{pmatrix} ACE_1 \\ ACE_2 \end{pmatrix} = (\phi_1 \ \ -\phi_2 \ \ 0 \ \ 0 \ \ 0 \ \ 1)\left(\Delta f_1 \ \ \Delta f_2 \ \ P_{DEG} \ \ P_{EV} \ \ P_{FC} \ \ \Delta P_1^{tie}\right)^T \tag{11}$$

The state space model defined in (10) and (11) can be represented in general form as (12)

$$\left\{ \dot{x}(t) = Ax(t) + Bu(t) + Dd_D(t) + Ed_{DG}(t)y(t) = Cx(t) \right. \tag{12}$$

Where $\boldsymbol{x} \in \mathbb{R}^6$ and $\boldsymbol{u} \in \mathbb{R}^3$ represent the vectors of the state variables and control signals respectively. While $\boldsymbol{d_D} \in \mathbb{R}^2$ and $\boldsymbol{d_{RES}} \in \mathbb{R}^2$ are the disturbance inputs from the changes in the load demand and the fluctuations from the RES respectively. The matrices *A, B, C, D,* and *E* are the coefficients matrices. The elements of the control vector, $\boldsymbol{\Psi} \in \mathbb{R}^3$ controls the DEG, EV and the FC. The generation rate of the DEG is constrained with a saturation of 9.8 $\%/min$. In the proposed MG, only the active powers of DEG, FC and EV are controllable and can participate in the LFC, since PV and WT are non-dispatchable.

3. MPC-based frequency controller

In this section, concept of model predictive control (MPC) is explained. In addition, the design of the MPC for the MG frequency control also is presented.

3.1. Concept of model predictive control

Generally, model predictive control (MPC) entails computing the solution of an online finite horizon optimal control problem by taking in to consideration the system dynamics (which can be linear or nonlinear) and constraints of the states, $\boldsymbol{x} \in \mathbb{R}^{n_x}$ and that of the controls, $\boldsymbol{u} \in \mathbb{R}^{n_u}$. It involves taking the present measurement at a continuous or discrete time to predict the future dynamic behavior of the system using its dynamic model over a prediction horizon N_p, and optimally generate the control input $\overline{u}$ over a control horizon N_c (with $N_\mathrm{p} \geq N_\mathrm{c}$), in order to optimize a pre-defined target objective, as illustrated in Fig. 4.

When the system reaches steady state, then $\overline{u}\left(\left[N_c, N_p\right]\right)$ is maintained as u, till another disturbance or a mismatch between the predicted output $\overline{y}$ and the set point occurred. As another scenario, when the optimization problem can be solved for infinite N_p and N_c, then u_0 ($u(0) = u_0$) can be applied to the system at time t ($\forall t \in [0, \infty]$).

However, this scenario can be difficult to be encountered in reality because of the disturbances and the output mismatch, the real system behavior is different from the predicted behavior. Thus, $\overline{u}$ is only implemented when the measurement in the next sampling time $\mathscr{k}$ is obtained, at time $t + \mathscr{k}$. Hence, the prediction and optimization (either deterministic or stochastic models) used to obtain $\overline{u}(t)$ is repeated to determine $\overline{u}(t + \mathscr{k})$, with N_p and N_c shifted ahead by $\mathscr{k}$. Due to the shifting of N_p and N_c, MPC is often regarded as moving horizon or receding horizon control.

It can be understood that MPC is governed by two basic operations; prediction and control optimization as shown in Fig. 3.

3.1.1. Model-based prediction

Unlike the rest of the feedback controllers that normally compute $\boldsymbol{u}(t)$ based on the information of the present state $\boldsymbol{x}(t)$ or preceding state $\boldsymbol{x}(t^-)$ information, MPC obtains $\overline{\boldsymbol{u}}(t)$ using both the predicted states $\boldsymbol{x}(t + \mathscr{k})$ starting from $\boldsymbol{x}(t)$.

3.1.2. Control optimization

After predicting the future dynamics of the system to be control, the MPC then optimizes a predefined objective function obtained from errors in measurements, subject to the constraints of $\boldsymbol{x}(t)$ and $\boldsymbol{u}(t)$.

(a) Online optimization

The predefined objective function that mathematically defines the target control performance is minimized online at each $\mathscr{k} \in \mathbb{Z}^+$. Depending on the control objective, the objective function can be integral squared error (ISE), integral solute error (IAE) or integral time absolute error (ITAE) of the difference between the predicted and the reference output, or that of an error between $\overline{\boldsymbol{u}}(t)$ and $\overline{\boldsymbol{u}}(t + \mathscr{k})$ or their combination. ISE is the most widely applied. In conventional MPC, the optimization is repetitively solved online using quadratic programing till certain stopping criteria is met. The repetition is to a large extent,

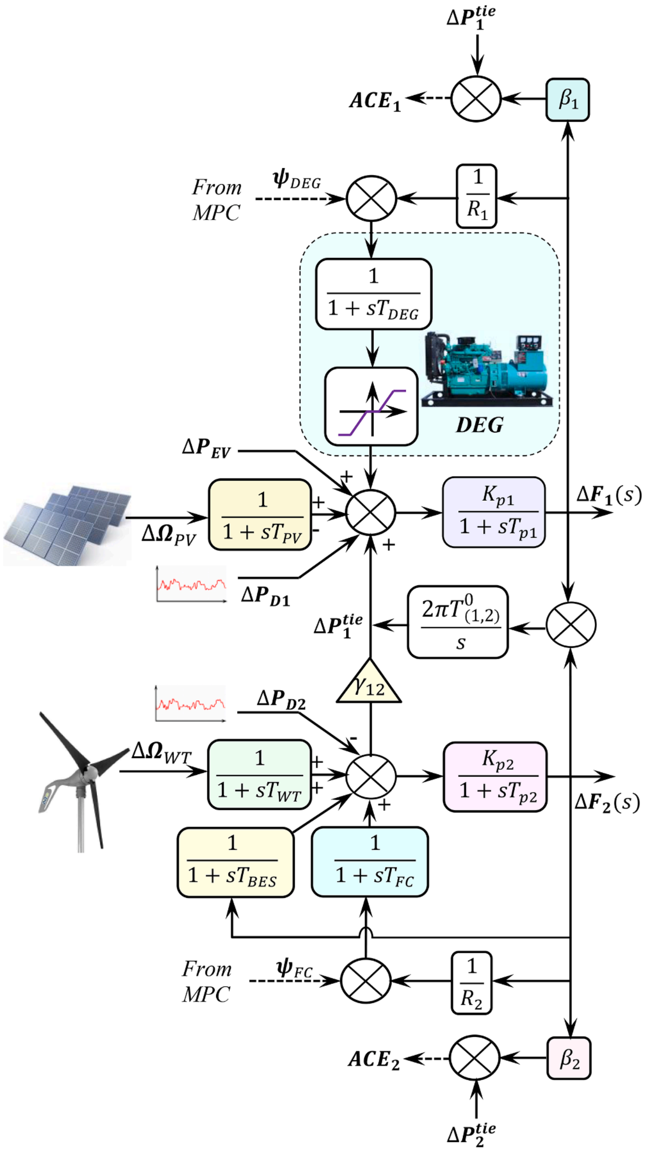

Fig. 3. Transfer function diagram of the proposed 2-CA MG.

reduce the model uncertainties and the difference between the real and predicted dynamics and thus, improve the control performance.

(b) Inputs, States and Controls Constraints

To guarantee the stability of the system, some logical dynamic conditions must be satisfied during the online optimization. These conditions, better referred as constraints can imposed on the inputs, states or the control variables. One peculiarity of MPC is that the constraints can be incorporated explicitly into the optimization problem, devoid of any transformation thereby leading to a less conservative solutions. In addition, since $\boldsymbol{x}(t+\mathscr{k})$ is obtained through prediction, then $\overline{\boldsymbol{u}}(t)$ can be implemented on the system to avert violating the states' constraints. Usually, there is a compromise between satisfying the constraints and obtaining an excellent control performance.

3.1.3. MPC on linear models

The formulation of MPC for linear and non-linear models differ since the model of the MG considered in this study is linearized (presented in the next Section), formulation of linear model is highlighted.

Consider a basic form of linear discrete state space in (12);

$$\boldsymbol{x}(\mathscr{k}+1)=A\boldsymbol{x}(\mathscr{k})+B\boldsymbol{u}(\mathscr{k})+\mathscr{F}\boldsymbol{d}(\mathscr{k}) \tag{13}$$

$$\boldsymbol{y}_{\ell}(\mathscr{k})=C_{\ell}\boldsymbol{x}(\mathscr{k}) \tag{14}$$

$$\boldsymbol{y}_{\mathscr{k}}(\mathscr{k})=C_{\mathscr{k}}\boldsymbol{x}(\mathscr{k}) \tag{15}$$

Where $\boldsymbol{d}\in\mathbb{R}^{n_d}$ is the measurable disturbance, $\boldsymbol{y}_{\ell}\in\mathbb{R}^{n_{\ell}}$ is the controlled output, and $\boldsymbol{y}_{\mathscr{k}}\in\mathbb{R}^{n_{\ell}}$ is the constrained output. The exact solution of the DEs is defined as

$$\dot{\boldsymbol{x}}(t)=A_{\zeta}\boldsymbol{x}(\mathscr{k})+B_{\zeta}\boldsymbol{u}(\mathscr{k})+\mathscr{F}_{\zeta}\boldsymbol{d}(\mathscr{k}) \tag{16}$$

The terms of (13) can be obtained using

$$A=e^{A_{\zeta}\mathscr{k}} \tag{17}$$

$$B=\int_0^{\mathscr{k}} e^{A_{\zeta}\delta}d\delta\cdot B_{\zeta} \tag{18}$$

$$\mathscr{F}=\int_0^{\mathscr{k}} e^{A_{\zeta}\delta}d\delta\cdot\mathscr{F}_{\zeta} \tag{19}$$

The optimization problem of linear MPC is formulated as

$$\min_{\Delta\boldsymbol{u}(\mathscr{k}:\mathscr{k}=1,\ ..\ N_c-1)} \boldsymbol{W}(\boldsymbol{x}(\mathscr{k}),\ \Delta\boldsymbol{u}(\mathscr{k}))$$

Where $\boldsymbol{W}$ is the MPC objective function. The online minimization of $\boldsymbol{W}$ is subject to inequality constraints in the control input vector, $\boldsymbol{u}(\mathscr{k})$, its increment, $\Delta\boldsymbol{u}(\mathscr{k})$ and the constrained output, $\boldsymbol{y}_{\mathscr{k}}$ defined as

$$\boldsymbol{u}_{min}\le\boldsymbol{u}(\mathscr{k}+t|\mathscr{k})\ \le\boldsymbol{u}_{max}, t=0,\ 1,\ 2,\ \ldots,N_c-1 \tag{20}$$

$$\Delta\boldsymbol{u}_{min}\le\Delta\boldsymbol{u}(\mathscr{k}+t|\mathscr{k})\ \le\Delta\boldsymbol{u}_{max}\ t=0,\ 1,\ 2,\ \ldots,N_c-1 \tag{21}$$

$$\boldsymbol{y}_{min}(\mathscr{k}+t)\le\boldsymbol{y}_{\mathscr{k}}(\mathscr{k}+t|\mathscr{k})\le\boldsymbol{y}_{max}(\mathscr{k}+t)\ t=0,\ \ldots,N_p \tag{22}$$

Where $\Delta\boldsymbol{u}(\mathscr{k})\ =\boldsymbol{u}(t+\mathscr{k})-\boldsymbol{u}(\mathscr{k})$, $\boldsymbol{u}_{min}$, $\boldsymbol{u}_{max}$, $\boldsymbol{y}_{min}$ and $\boldsymbol{y}_{max}$ are the minimum and maximum limits of the control input vector and the constrained output.

3.2. Frequency controller design

The proposed LFC has centralized architecture with an MPC as the central controller. Hence, the control actions in CA-1 are considered as external disturbance in CA-2 and vice-versa, as against a decentralized LFC which is completely decoupled. The design of the controller consists of the Kalman filter (KF) design and that of the rolling optimization of the MPC.

3.2.1. Kalman filter design

As a model-based controller, the MPC requires comprehensive knowledge of the entire dynamic system to be controlled. To achieve effective control, the MPC needs full state information from both CAs of the CAs. Among the well-known methods for obtaining the state

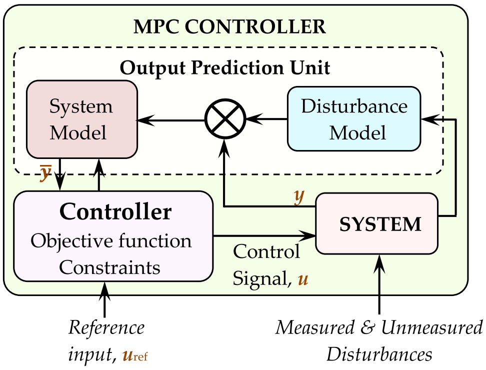

Fig. 4. Concept of model predictive controller.

information are:-

i. Transmitting all the state information over communication channels to the controller [36],
ii. Estimating the states locally by means of observer by processing the previous local signals [32].

The first method is more expensive due to the requirement of the fast communication link. In addition, not all state variables are directly accessible and those that are accessible often contain noise. Therefore, a Kalman Filter (KF) is utilized as an observer to estimate the unmeasurable state variables accurately. The estimation takes the measurable variables considering the noises associated with measurements.

The MG model expressed in (12) is with the assumption that all the state variable are measurable and accessible to the MPC. To design the KF, the discrete-time model of (12) is modified to include the measurement noises as in (23)

$$\begin{gathered}\boldsymbol{x}(\mathscr{k}+1)=A\boldsymbol{x}(\mathscr{k})+B\boldsymbol{u}(\mathscr{k})+D\boldsymbol{d}_{\boldsymbol{D}}(\mathscr{k})+D\boldsymbol{d}_{\boldsymbol{DG}}(\mathscr{k})+\chi_n\boldsymbol{\xi}(\mathscr{k})\\ \boldsymbol{y}(\mathscr{k})=C\boldsymbol{x}(\mathscr{k})+\mathfrak{z}(\mathscr{k})\end{gathered} \tag{23}$$

Where ξ and $\mathfrak{z}$ are the Gaussian pseudo-white measurement noises with covariance matrices W_{kf} and V_{kf} respectively defined as,

$$W_{kf}=\mathrm{E}\left\{\boldsymbol{\xi}(\mathscr{k}).\boldsymbol{\xi}(\mathscr{k}+1)^T\right\}\geq 0; \tag{24}$$

$$V_{kf}=\mathrm{E}\left\{\mathfrak{z}(\mathscr{k}).\mathfrak{z}(\mathscr{k}+1)^T\right\}>0; \tag{25}$$

$$\mathrm{E}\left\{\boldsymbol{\xi}(\mathscr{k}).\boldsymbol{\xi}(\mathscr{k}+1)^T\right\}=0; \tag{26}$$

The KF is designed with the assumption that the pair (A, C) is detectable and observable and V_n is invertible.

Definition 1. (*Observability*): The system model, (12) modified to (23) with the pair (A, C) is observable if and only if for any initial state, $\boldsymbol{x}(\mathscr{k}_0)$ and any final state, $\boldsymbol{x}(\mathscr{k}_n)$; $n=0,\ 1,\ 2,\ \ldots,\ i-1$, there exists an input sequence $\boldsymbol{u}(\mathscr{k}_0), \boldsymbol{u}(\mathscr{k}_1),\ \ldots,\ \boldsymbol{u}(\mathscr{k}_n)$, which relate uniquely $\boldsymbol{x}(\mathscr{k}_0)$ to $\boldsymbol{x}(\mathscr{k}_n):n\in\mathbb{R}^{n_i}$.

Definition 2. (*Detectability*): For an unmeasured state $\boldsymbol{x}(\mathscr{k}_n)$, the system in (11) with the pair (A, C) is detectable if and only if for any measured control input $\boldsymbol{u}(\mathscr{k}_n)$, and output $\boldsymbol{y}(\mathscr{k}_n)$; $n=0,\ 1,\ 2,\ \ldots,\ i-1$, there exist an estimated state $\widetilde{\boldsymbol{x}}(\mathscr{k}_n)$ such that $\|\ \boldsymbol{x}(\mathscr{k}_n)-\widetilde{\boldsymbol{x}}(\mathscr{k}_n)\| \rightarrow 0$.

From the definitions, it implies that if a system is observable, then it is detectable, even though the converse is not necessarily be applicable.

The KF is modelled based on a function of the estimated state variables $\widetilde{\boldsymbol{x}}(\mathscr{k})$ defined in (27). With the application of the estimated output $\widetilde{\boldsymbol{y}}(\mathscr{k})$, the state space model for the KF is expressed in (24):

$$\Gamma_{kf}=\lim_{\mathscr{k}\rightarrow\infty}E\left\{(\boldsymbol{x}(\mathscr{k})-\widetilde{\boldsymbol{x}}(\mathscr{k}))^T C^T C(\boldsymbol{x}(\mathscr{k})-\widetilde{\boldsymbol{x}}(\mathscr{k}))\right\} \tag{27}$$

$$\dot{\widetilde{\boldsymbol{x}}}(\mathscr{k})=A\widetilde{\boldsymbol{x}}(\mathscr{k})+K_{kf}(\boldsymbol{x}(\mathscr{k})-\widetilde{\boldsymbol{x}}(\mathscr{k}))\ \widetilde{\boldsymbol{y}}(\mathscr{k})=C\widetilde{\boldsymbol{x}}(\mathscr{k}) \tag{28}$$

Where K_{kf} is the gain of the KF obtained from one of the solutions of the Algebraic Riccati Equation presented in [39]. The solution is based on the following theorem.

Theorem. Suppose that pair (A, C) is detectable and that $\Gamma_{kf}^0=\mathscr{O}$. Then the solution of (27) converges to a non-negative definite matrix $\vec{\Gamma}$ as $\mathscr{k}\rightarrow\infty$ and $\vec{\Gamma}$ satisfies the equation

$$\mathfrak{z}_{kf}A^T+\mathfrak{z}_{kf}A+\xi^T W_{kf}\xi-\mathfrak{z}_{kf}C^T\sigma C\mathfrak{z}_{kf}=0 \tag{29}$$

The KF gain is subsequently obtained using (30),

$$K_{kf}=\mathfrak{z}_{kf}C^T\sigma \tag{30}$$

3.2.2. *Controller online optimization*

The MPC optimization minimized a weighted function comprising of squared tracking errors and control inputs sampled over discrete time $\mathscr{k}$, as expressed in (31),

$$\begin{gathered}\min_{\psi(\mathscr{k}:\mathscr{k}=1,\ ..\ N_c-1)} W_i\ \text{ Such that}\\ W_i(\mathscr{k})=\sum_{k=1}^{N_p}\left(\boldsymbol{ACE}(\mathscr{k})-ACE_{ref}(\mathscr{k})\right)^T\boldsymbol{\mu}\left(\boldsymbol{ACE}(\mathscr{k})-ACE_{ref}(\mathscr{k})\right)+\sum_{k=1}^{N_p}\boldsymbol{\psi}(\mathscr{k}-1)^T\boldsymbol{\Omega}\boldsymbol{\psi}(\mathscr{k}-1)\end{gathered} \tag{31}$$

Where $\boldsymbol{ACE}=(ACE_1\quad ACE_2)^T$, and $\boldsymbol{\psi}=(\boldsymbol{\psi}_{DEG}\quad \boldsymbol{\psi}_{EV}\quad \boldsymbol{\psi}_{FC})^T$ are the output and control signal vectors respectively, whose positive definite and symmetric weighting matrices are defined as $\boldsymbol{\mu}$ and $\boldsymbol{\Omega}$. They are fine-tuned to improve the dynamic performance of the MPC. N_c and N_p are the prediction and control horizons are respectively.

The minimization of (31) was carried out subject to some system and dynamic constraints, among which are;

- *Generation rate*: due to inertia of the DEG, the rate at which P_{DEG} is changing due to ψ_{DEG} is constrained to $\mathrm{GRC_{DEG}}$ take as $\pm 8.5\ \%/min$,
- *Frequency deviation:* f_1 and f_2 are restricted within certain limits as expressed in (32) to preserve the MG stability.

  $$|\Delta f_i|\leq\Delta f_i^{max}\ :\ i=1,\ 2 \tag{32}$$

- *RoCoF*: the rate of change of frequency (RoCoF), expressed in (33), is constrained to a limit ±0.5Hz/s [40], to avoid abrupt changes in the area frequencies following a disturbances,

  $$RoCoF_i=\frac{f_i(\mathscr{k}+1)-f_i(\mathscr{k})}{d\mathscr{k}} \tag{33}$$

The proposed LFC is designed with centralized architecture, as shown in Fig. 5. This control structure is chosen to its ability to coordinate and optimize the entire system's performance by managing both CAs from a single point of control. This holistic view allows it to simultaneously monitor and regulate both local state variables, $\boldsymbol{x}_\mathbf{i}$, (for ith CA) and global interactions with its neighbouring jth CA, $\boldsymbol{x}_{\boldsymbol{j}}$. By having access to system-wide data, a centralized controller can make

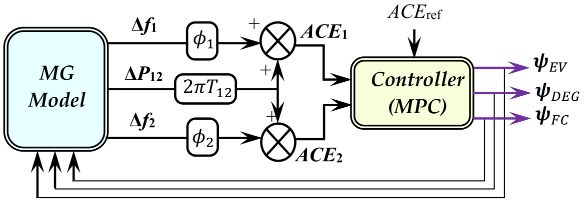

Fig. 5. Structure of the proposed frequency controller.

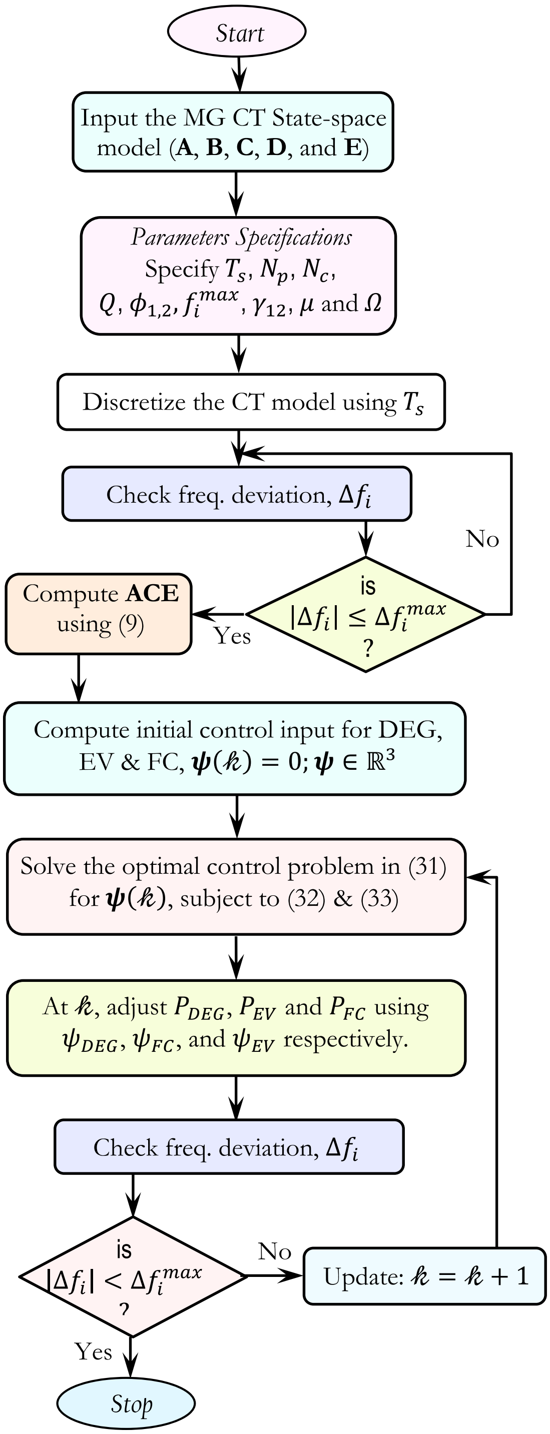

Fig. 6. Flowchart of the proposed frequency control scheme.

more informed decisions, ensuring optimal adjustments across all subsystems. Furthermore, centralized control can quickly respond to large disturbances affecting multiple areas, providing a more comprehensive and robust approach to maintaining grid reliability compared to decentralized scheme.

As depicted in Fig. 5, the MPC uses the ACEs from both CAs and a predefined reference error (ACE_{ref}), and optimize (31) to generate the optimal signals for the EV, DEG and the FC.

The generated control signal ψ_{DEG} regulates the diesel intake of the DEG, ψ_{FC} regulates the hydrogen intake of the FC, while ψ_{EV} controls the charge/discharge of the available EVs through the aggregator. Fig. 6 shows the flowchart of the proposed frequency control scheme

3.2.3. *Input-to-state stability analysis*

Local Input to State Stability (ISS), which can be understood as a robustness property of the asymptotic stability of the system equilibrium, and providing estimates of the ISS gains. The system model (12) is analysed to ensure that it is input-to-state stable.

Definition 3. (Input-to-State Stability): A system (12) (discretized at $\mathscr{k}$ sampling time) is locally and uniformly input-to-state stable if there exists a class $\phi \in \kappa\mathscr{L}$, and $\vartheta \in \kappa_\infty$, so that for any $\boldsymbol{x}(\mathscr{k}_0)$ and $\boldsymbol{u}(\mathscr{k}_n)$:$\forall \mathscr{k} \geq 0; \boldsymbol{n} \in \mathbb{Z}^+$ the solution satisfies

$$|\boldsymbol{x}(\mathscr{k}_n)| \leq \phi(\ \| \boldsymbol{x}(\mathscr{k}_0)\|, \mathscr{k}_n - \mathscr{k}_0\ ) + \vartheta(\ \| \boldsymbol{u}(\mathscr{k}_n)\|_\infty) \tag{34}$$

The function ϑ is said to be κ function if it is continuous and strictly increasing with $\vartheta(0) = 0$. By extension, the function is κ_∞ function if $lim_{\mathscr{k}_n \to \infty}\{\vartheta(\mathscr{k}_n)\} \to \infty$. Similarly, function ϕ in (30) is $\kappa\mathscr{L}$ function if for each $\mathscr{k}_n \geq 0$, the function $\vartheta(\cdot, \mathscr{k}_n)$ is κ function and $\vartheta(s, \mathscr{k}_n)$ is monotonically decreasing with respect to $\mathscr{k}_n$ implying that $lim_{\mathscr{k}_n \to \infty}\{\vartheta(\mathscr{k}_n)\} \to 0$.

For the system in (12) to meet up with the ISS condition, the state matrix A should have eigenvalues with negative real parts. Thus, it is stable if the spectral radius, $\rho(A) < 1$. From the general solution of the discretized system (12),

$$x(\mathscr{k}_n) = A^{\mathscr{k}_n} x(\mathscr{k}_0) + \sum_{j=\mathscr{k}_0}^{\mathscr{k}_n - 1} A^j B \tag{35}$$

For some constants $\Omega > 0$ and $0 \leq \lambda < 1$, it implies that

$$\| A^{\mathscr{k}_n} x(\mathscr{k}_0) \| \leq \Omega \lambda^{\mathscr{k}_n} \| x(\mathscr{k}_0) \| \tag{36}$$

By extension, the summation implies that

$$\sum_{j=\mathscr{k}_0}^{\mathscr{k}_n - 1} \Omega \lambda^{\mathscr{k}_n} \| B \| \leq \Omega M \sum_{j=\mathscr{k}_0}^{\mathscr{k}_n - 1} \lambda^{\mathscr{k}_n} \tag{38}$$

The geometric series summation in (38) can be expressed as

$$\sum_{j=\mathscr{k}_0}^{\mathscr{k}_n - 1} \lambda^{\mathscr{k}_n} = \frac{1 - \lambda^{\mathscr{k}_n}}{1 - \lambda} \tag{39}$$

Combining (35) - (39),

$$x(\mathscr{k}_n) = \Omega \lambda^{\mathscr{k}_n} \| x(\mathscr{k}_0) \| + \frac{\Omega M}{1 - \lambda} \tag{40}$$

From the definition in (36),

$$\phi(\ \| \boldsymbol{x}(\mathscr{k}_0)\|, \mathscr{k}_n\ ) = \Omega \lambda^{\mathscr{k}_n} \| x(\mathscr{k}_0) \| \ \forall \mathscr{k} \geq 0;\ \boldsymbol{n} \in \mathbb{Z}^+ \tag{41}$$

Similarly,

$$\vartheta(\ \| \boldsymbol{u}(\mathscr{k}_n)\|_\infty) = \frac{\Omega \| \boldsymbol{u}(\mathscr{k}_n)\|_\infty}{1 - \lambda} \tag{42}$$

Since for any bounded control input, $\boldsymbol{u}(\mathscr{k}_n)$, the state variable $\boldsymbol{x}(\mathscr{k}_n)$ remains bounded, it can be deduced that the system in (12) is ISS.

Table I
System parameters.

Parameter	Value	Parameter	Value
γ_{12}	*1*	$\boldsymbol{T_{PV}}$	*0.35* s
ϕ_1	*0.46* puMW/Hz	$\boldsymbol{T_{BES}}$	*0.35* s
ϕ_2	*0.44* puMW/Hz	$\boldsymbol{T_{EV}}$	*0.75* s
$\boldsymbol{K_{EV}}$	122 *Hz/MW*	T_{DEG}	1.72 s
$\boldsymbol{K_{EV}}$	82 *Hz/MW*	T_{FC}	0.45 s
T_{p1}	*20* s	$2\boldsymbol{\pi T}^0_{(1,\ 2)}$	*0.545* puMW/Hz
T_{p2}	*22* s	$\boldsymbol{GRC_{DEG}}$	±*8.5* %/min

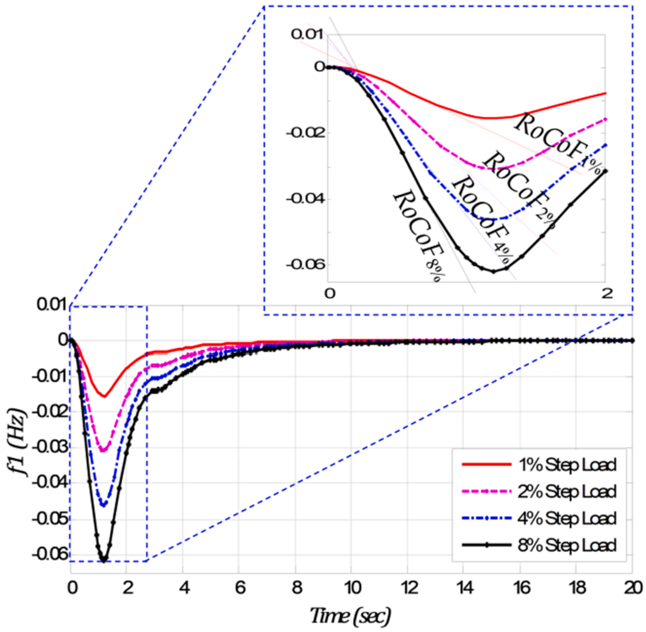

Fig. 7. Δf1 with step load variations.

4. Results and discussion

To establish the effectiveness of the proposed on the LFC, the two area MG is simulated with step and random disturbances. The time-based simulation study is carried out to demonstrate the performance of the EV (through the aggregator) only mitigating the frequency fluctuations by reducing the RoCoF. The study is carried out in MATLAB/Simulink® on an Intel(R) Core(TM) i5-6200U CPU 2.40 GHz computer. The system parameters are summarized in Table I.

4.1. Selection of MPC horizons

As MIMO system, the MG is controlled using the three optimal signals; ψ_{DEG}, ψ_{FC} and ψ_{EV} serving as the input. While disturbances are established through the disturbances inputs $\boldsymbol{d_D}$ and $\boldsymbol{d_{RES}}$.

Ideally, best control performance is obtained using the MPC if $N_P\rightarrow\infty$ and $N_C\rightarrow\infty$. With the large N_p, the MPC considers long-term effects of current control actions $(\boldsymbol{u}(k_n):\ \forall k \geq 0)$, leading to more accurate and optimal control. In addition, As N_c increases, the MPC gains the flexibility to plan further into the future, leading to potentially better long-term performance [30]. However, these come with significant trade-offs. Large N_p and N_c increase the computational complexity. In particular, large N_p value makes the system more sensitive to modeling errors or disturbances, which can propagate further in time. Thus, in either scenarios presented in this study, finite values of N_p and N_c are carefully selected to strike balance between computational efficiency and control performance. The symmetric weighting matrices for the tracking errors and control inputs $\boldsymbol{\mu}$ and $\boldsymbol{\Omega}$ (both positive definite) are then defined;

Tracking errors weighting matrices: $\mu = 1\ \times I_{N_p\times N_p}$ $(\boldsymbol{\mu} \succ \mathbf{0})$
Control input weighting matrices: $\Omega = 0.5\ \times I_{N_c\times N_c}$ $(\boldsymbol{\Omega} \succ \mathbf{0})$.

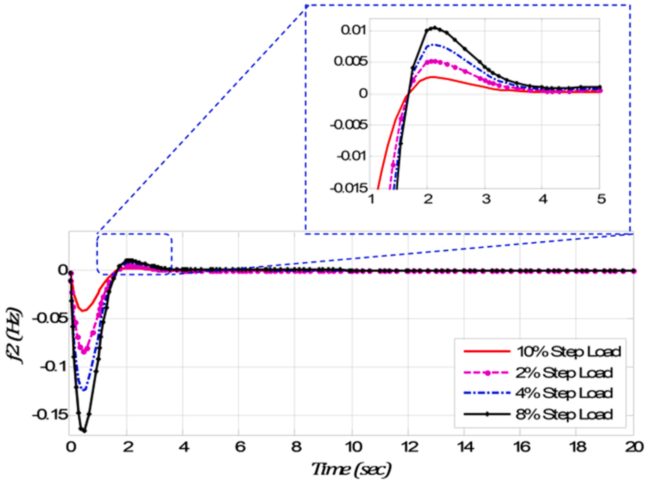

Fig. 8. Δf2 with step load variations.

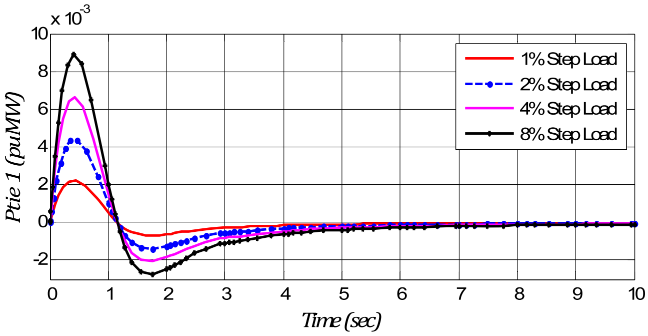

Fig. 9. ΔP_1^{tie} under different loading conditions.

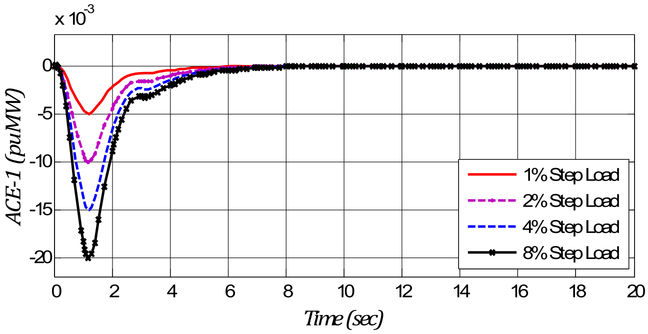

Fig. 10. ACE1 with step load variations.

4.2. Response to step load variations

To investigate the impact of loading on the LFC, the MG is subjected to an increasing load changes, and their effects on the LFC are studied. CA_2 of the MG is subjected to 1 %, 2 %, 4 %, and 8 % step load changes. Only the DEG, FC and EV are made to participate in the LFC, as such the WT and PV are excluded from the frequency support.

In this scenario, N_p and N_c are set to 85 and 10 respectively, after an iterative tuning process. These values were selected to achieve a balance between computational efficiency and control performance. In addition, the frequencies in the respective CAs are constrained to ±0.2 Hz.

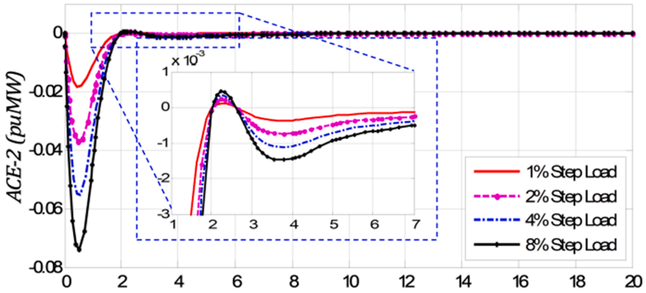

Fig. 11. ACE2 with step load variations.

Table II

summary of the responses under/overshoots under different loading conditions.

Step load	Freq. dev. (Hz)		Tie-line power dev.		ACE (puMW)	
	Δf_1	Δf_2	$\Delta \boldsymbol{P}_1^{tie}$	ΔP_2^{tie}	ACE_1	ACE_2
1 %	-0.0172	-0.0446	2.03×10^{-3}	-2.03×10^{-3}	$\mathbf{5.01 \times 10^{-3}}$	**0.0198**
2 %	-0.0306	-0.0724	4.14×10^{-3}	-4.14×10^{-3}	10.25×10^{-3}	0.0382
4 %	-0.0485	-0.1270	6.52×10^{-3}	-6.52×10^{-3}	15.20×10^{-3}	**0.0566**
8 %	-0.0622	-0.1761	9.23×10^{-3}	-9.23×10^{-3}	20.05×10^{-3}	**0.0725**

Table III

Comparative analysis on system dynamic characteristics.

Controller	Δf_1(Hz)	Δf_2(Hz)	$\Delta \boldsymbol{P}_1^{tie}$(pu)
H_2/H_∞, [8]	-0.0485	-0.127	$\boldsymbol{6.52 \times 10^{-3}}$
QORSA-based FOID [23]	-0.0425	-0.112	$\boldsymbol{4.22 \times 10^{-3}}$
AO-based PID [24]	-0.0310	-0.080	$\boldsymbol{4.53 \times 10^{-3}}$
CSA-based FOPID [22]	-0.0410	-0.077	$\boldsymbol{5.28 \times 10^{-3}}$
ANFIS/ANN based [27]	-0.0600	-0.057	$\boldsymbol{4.58 \times 10^{-3}}$
PSO-based FOPID [17]	-0.0485	-0.126	–
MFO-based LQR/PI [18]	-0.0688	-0.0642	$\boldsymbol{4.56 \times 10^{-3}}$
Dec-MPC [35]	-0.0410	-0.039	$\boldsymbol{5.26 \times 10^{-3}}$
SCA-based FOPID [12]	-0.0459	-0.0422	$\boldsymbol{6.38 \times 10^{-3}}$
Proposed	**-0.0306**	**-0.0524**	4.14×10^{-3}

It is demonstrated from the $\boldsymbol{\Delta f}$ responses shown in Figs. 7 and 8, that the MPC has only not the restored the frequency to near zero deviation, but also constrained to the specified limits.

For instance, the $RoCoF_1$ of -0.021Hz/sec, -0.042Hz/sec, -0.086Hz/sec, and -0.174Hz/sec following the 1 %, 2 %, 4 %, and 8 % step load changes respectively. It is observed that the maximum *RoCoF* of 0.2Hz/sec is not violated.

Similar observation is made in $RoCoF_2$. Even though the developed MPC–based scheme is capable of suppressing the effect of the load changes in both CAs, however, the fluctuations in $\boldsymbol{\Delta f_2}$ are eliminated faster compared to that of $\boldsymbol{\Delta f_1}$. This is largely due to the faster response of BESS in CA_2 in comparison to the DEG in CA_1. Similar observation can be realised in the $\Delta \boldsymbol{P}_1^{tie}$ and $\boldsymbol{ACE}$ responses, shown in Figs. 9–11.

Moreover, it is observed that the loading has more effect on the undershoots than the settling time, since the latter depends on the controller speed and response of the frequency supporting facility. Since the MG has only two CAs, the $\Delta \boldsymbol{P}_1^{tie}$ and $\Delta \boldsymbol{P}_2^{tie}$ are identical with opposite direction of the. Table II summarizes the under/overshoots of the state variables under different loading conditions.

To evaluate the superior performance of the developed controller, the responses of the system are compared with responses obtained using other control schemes, as summarized in Table III. As a basis for the comparison, the MG is perturbed with 2 % step load increase in one of the CAs, in all the scenario considered for the comparative analysis.

While various control methods successfully restore frequencies to nominal values with reduced nadir and steady-state error, the proposed MPC-based scheme has generally demonstrated superior performance. However, certain schemes, such as Dec-MPC and SCA-based FOPID, achieved better frequency responses in CA-2, with nadirs of -0.039 *Hz* and -0.0422 *Hz*, respectively. This can be attributed to the fact that greater emphasis is placed on minimizing $\boldsymbol{\Delta f_i}$ than on $\Delta \boldsymbol{P}_{\mathbf{i}}^{\mathbf{tie}}$ while tuning the controllers. From Table III, it is seen that despite the smaller undershoots in $\Delta \boldsymbol{f_2}$ obtained using these schemes, yet the $\Delta \boldsymbol{P}_{\mathbf{2}}^{\mathbf{tie}}$ undershoots are found to be larger than that of the proposed scheme. It is understood that overemphasizing frequency deviation minimization can therefore come at the expense of tie-line power performance.

The Dec-MPC scheme effectively reduces the $\boldsymbol{f_i}$ by focusing on local frequency stability, but its decentralized control architecture limits its ability to adequately manage the $\boldsymbol{P}_{\mathbf{i}}^{\mathbf{tie}}$ dynamics. The lack of coordination between decentralized controllers in Dec-MPC prevents optimal adjustment of $\boldsymbol{P}_{\mathbf{i}}^{\mathbf{tie}}$, leading to its larger undershoots.

Furthermore, the proposed scheme only stabilized the area

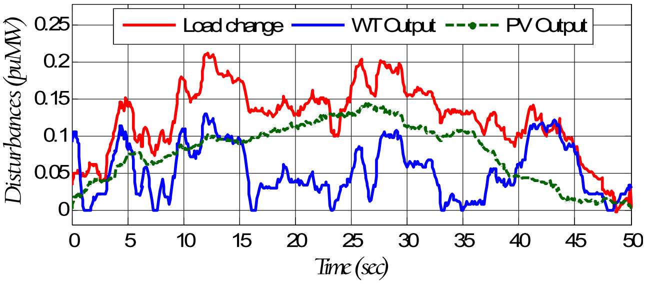

Fig. 13. Change in the load demand, PV and WT powers.

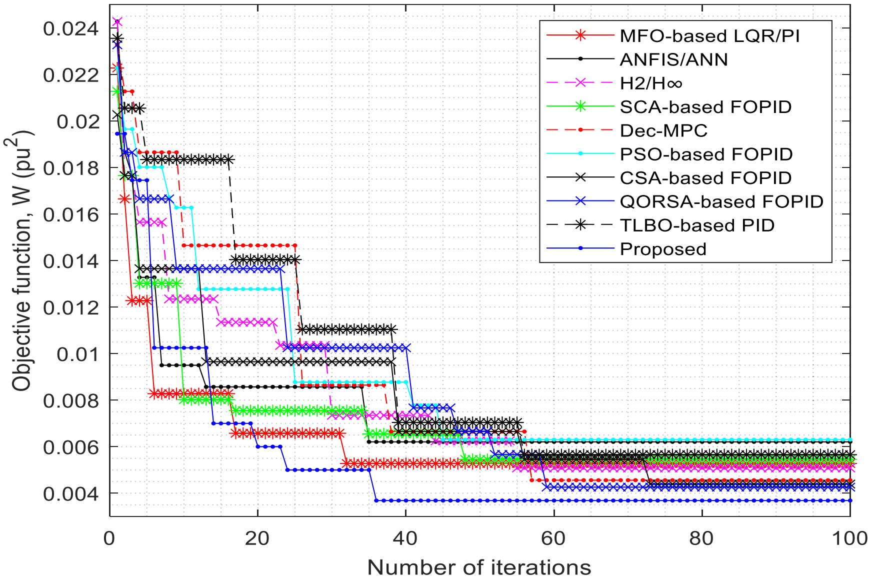

Fig. 12. Convergence curves.

frequencies and tie-line power with lower nadirs and significant reduction in their settling times, but also converges faster than the other control schemes, as shown by the convergence curves for 100 iterations in Fig. 12. This is due to the effective constraint handling capability of the MPC controller couples with the careful selection of the $\boldsymbol{N}_{\mathbf{p}}$, $\boldsymbol{N}_{\mathbf{c}}$, $\boldsymbol{\mu}$ and $\boldsymbol{\Omega}$.

4.3. Response to step load variations

To assess the participation of the EV fleet in the LFC and the MG dynamic behavior in a more realistic setting, the MG is subjected to a random disturbance due to the fluctuations in the change in the load demand and the generations from RES shown in Fig. 13 respectively limits.

As in the previous case, after an iterative tuning process, the N_{p} and N_{c} are set to 92 and 15 respectively. These values were carefully selected to optimize the balance between computational efficiency and control performance. Furthermore, the frequency deviations in the respective CAs are constrained to ±0.02Hz while the RoCoFs are constrained to ±0.02Hz/s. While designing the controller, the following were assumptions considered;

i. Due to the stochastic nature of the charging pattern, it is assumed that the EV is available at any instant, ensuring that the power limits P_{EV}^{min} and P_{EV}^{max} are not exceeded,
ii. The communication delay between the DEG, FC and EV with the MPC controller is assumed to be negligible, thus, the control actions by the signals; ψ_{DEG}, ψ_{FC} and ψ_{EV} are promptly executed.
iii. At the beginning of the simulations, the initial conditions for all the system states, $\{\boldsymbol{x}(\mathscr{k}_0) = 0 : \ \forall \boldsymbol{x}_n\}$ are set zero ensuring that no residual responses in the system prior to applying the MPC.

With these assumptions, the MPC controller is applied to stabilize the frequency in both areas. The EV, DEG and FC are made to respond to the load change and minimize the frequency fluctuations instantly. Therefore, the MPC generated the $\boldsymbol{\psi}_{\mathrm{EV}}$, $\boldsymbol{\psi}_{\mathrm{DEG}}$, and $\boldsymbol{\psi}_{\mathrm{FC}}$ (shown in Figs. 14–16) to optimally adjust the output powers of these micro-sources.

To assess the effectiveness of the proposed scheme in this scenario, the responses obtained the under random disturbances are compared with other control schemes.

Figs. 17 and 18 show the trajectories of $\boldsymbol{\Delta f_1}$ and $\boldsymbol{\Delta f_2}$. For clarity sake, among the schemes used for the comparative analysis, only responses obtained using Dec-MPC and SCA-based FOPID (identified to have superior performance than the rest of the methods in the previous scenario) are shown.

The results demonstrate that the proposed control scheme achieves fewer oscillations compared to the other methods, indicating a more stable system response which is critical for maintaining reliability under varying load conditions. The trajectories clearly show that the proposed scheme successfully kept $\boldsymbol{\Delta f}$ within the predefined limit of ±0.02 Hz, highlighting its strong constraint-handling performance. Although the Dec-MPC scheme also showed effective constraint management, it slightly breached the $\boldsymbol{\Delta f_2}$ constraint. In contrast, most other schemes, such as the SCA-based FOPID, significantly violated the constraint in both CAs. This can be attributed to the poor constraint-handling capabilities of PID controller.

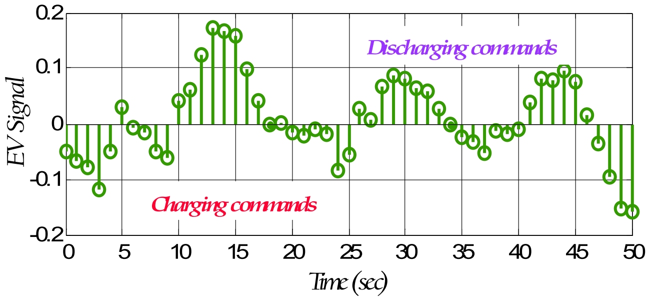

Fig. 14. ψ_{EV} with random disturbance.

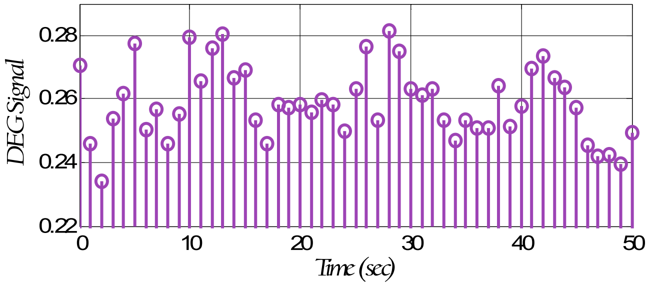

Fig. 15. ψ_{DEG} with random disturbance.

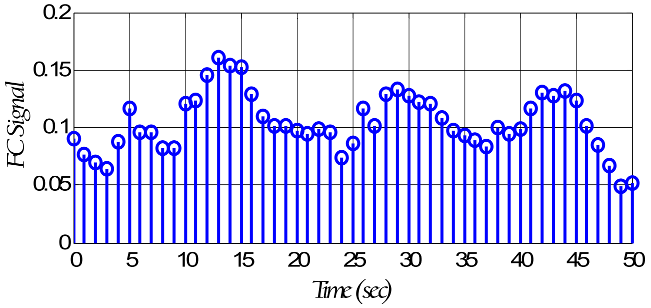

Fig. 16. ψ_{FC} with random disturbance.

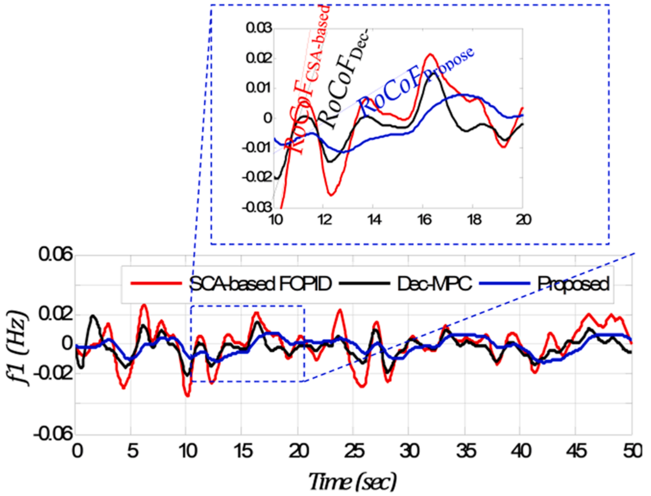

Fig. 17. $\boldsymbol{\Delta f_1}$ with random disturbance.

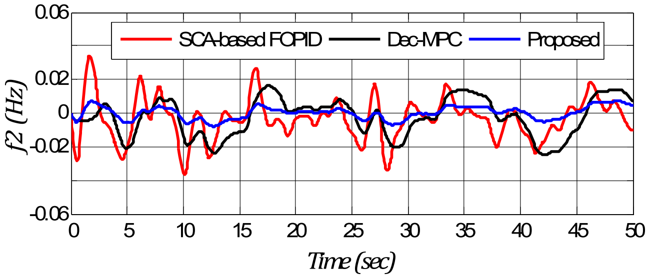

Fig. 18. $\boldsymbol{\Delta f_2}$ with random disturbance.

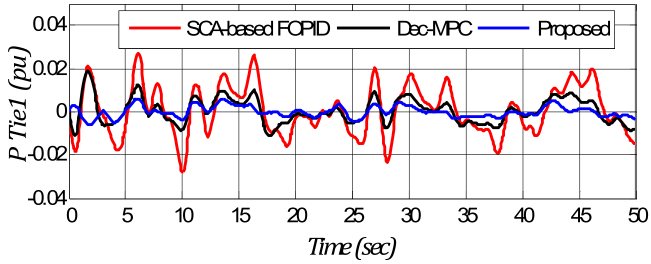

Fig. 19. ΔP_{12}^{tie} with random load demand.

Furthermore, the RoCoF of the system responses was also analyzed. At 10.7 s of simulation time, the proposed scheme achieved a $RoCoF_1$ of 0.005 *Hz/sec*, as shown in the zoomed-in section of Fig. 16. In comparison, the Dec-MPC and SCA-based FOPID stabilized the frequency with $RoCoF_1$ values of 0.025*Hz/sec* and 0.036*Hz/sec*, respectively. This demonstrates the superior ability of the proposed scheme to stabilize frequency with fewer abrupt changes, underscoring its efficacy in ensuring smoother frequency regulation. Similar observation is made in the $\boldsymbol{P}_{\mathrm{i}}^{\mathrm{tie}}$ responses as shown in Fig. 19.

In addition to stabilizing the area frequencies and tie-line power with lower nadirs and significantly reduced settling times, the proposed scheme demonstrated faster convergence compared to the other control methods. This improved performance is attributed to the MPC's robust constraint-handling capability, combined with its iterative tuning.

5. Conclusion

The study employed a finite horizon MPC strategy for LFC in a two-area islanded MG integrated with EV charging stations. A key challenge in such systems is the inherent variability of RES and unpredictable load fluctuations, which can significantly impact frequency stability. To address this, the proposed MPC-based control scheme was rigorously evaluated under two scenarios: step load changes and random disturbances from RES and load variations. The results demonstrated that the MPC-based LFC effectively mitigates the adverse effects of these fluctuations, maintaining frequency deviations within predefined limits while minimizing tie-line power oscillations. Compared to conventional approaches such as Dec-MPC and SCA-FOPID, the proposed controller exhibited superior robustness, handling random disturbances with faster convergence and reduced oscillations. Additionally, it significantly limited RoCoF, ensuring a more stable and resilient MG operation. By efficiently coordinating power adjustments from dispatchable sources and EV aggregators, the proposed approach enhances frequency stability and system reliability, making it a vital solution for modern MGs where RES penetration and load uncertainty pose major operational challenges. As future research, the stochastic nature of the EV can be incorporated while modelling the MG as well as the controller.

CRediT authorship contribution statement

Abdullahi Bala Kunya: Writing – original draft, Software, Methodology, Conceptualization. **Muhamad M. Mundu:** Project administration, Formal analysis, Data curation. **Aminu Babangida:** Investigation, Formal analysis. **Péter Tamás Szemes:** Writing – review & editing, Supervision, Funding acquisition.

Declaration of competing interest

The authors declare that they have no known competing financial interests or personal relationships that could have appeared to influence the work reported in this paper. We have nothing to declare.

Data availability

Data will be made available on request.

References

[1] S. Iqbal, F.A. Limon, M. Kabir, Z. Hossain, F. Jubayer, J.A. Soeb, A hybrid optimization algorithm based on cascaded (1 + PI)-PI-PID controller for load frequency control in interconnected power systems, Results Eng. 24 (1) (2024) 103624.
[2] D.P. Kothari, I.J. Nagrath, Automatic generation and voltage control. Modern Power System Analysis, Tata McGrawHill Education PrivateLimited, Delhi, 2003, pp. 290–325.
[3] A.J. Wood, B.F. Wollenberg, G.B. Sheblé, Control of Generation. Power Generation, Operation and Control, Wiley, USA, 2013, pp. 468–500.
[4] A. Abazari, H. Monsefa, B. Wu, Coordination strategies of distributed energy resources including FESS, DEG, FC and WTG in load frequency control scheme of hybrid isolated micro-grid, Electr. Power Energy Syst. 109 (1) (2019) 535–547.
[5] K. Torabi-Farsani, N. Vafamand, R. Razavi-Far, M. Saif, Secure frequency regulation of electric vehicle-connected microgrid system under multiple latency attacks, Comput. Electr. Eng. 101 (2022) 1–15.
[6] Y. Astriani, G. Shafiullah, M. Anda, H. Hilal, Techno-economic evaluation of utilizing a small-scale microgrid, in: Proceedings of the 10th International Conference on Applied Energy (ICAE2018), Hong Kong, China, 2018.
[7] IEA, "Global Electric Vehicle Outlook 2022," International Energy Agency, 2022. [Online]. https://www.iea.org/reports/global-ev-outlook-2022. [Accessed Oct. 2022].
[8] M. Khan, H. Sun, Y. Xiang, D. Shi, Electric vehicles participation in load frequency control based on mixed H2/H, Electr. Power Energy Syst. 125 (2021) 1–11.
[9] S.K. Nisha, N.S. Dattatraya, N.G. Jayalakshmi, Operation and control of multiple electric vehicle load profiles in bipolar microgrid with photovoltaic and battery energy system, J. Energy Storage 57 (2023) 1–18.
[10] W. Mo, P.D. Walker, N. Zhang, Dynamic analysis and control for an electric vehicle with harpoon-shift synchronizer, Mech. Mach. Theory. 133 (2019) 750–766.
[11] A. Khalila, Z. Rajaba, A. Alfergania, O. Mohamed, The impact of the time delay on the load frequency control system in microgrid with plug-in-electric vehicles, Sustain. Cities Soc. 35 (2017) 365–377.
[12] S. Pahadasingh, C. Jena, C.K. Panigrahi, SCA based load frequency control incorporating electric vehicle using cascaded controller, in: Proceedings of the 1st International Conference on Power Electronics and Energy (ICPEE-2021), Bhubaneswar, Odisha, India, 2021.
[13] S. Kaur, T. Kaur, R. Khanna, Design of the ANFIS based optimized frequency control module for an electric vehicle charging station, Appl. Energy 326 (2022) 1–13.
[14] S. Debbarma, A. Dutta, Utilizing Electric vehicles for LFC in restructured power systems using fractional order controller, IEEE Trans. Smart Grid (2016) 1–11, https://doi.org/10.1109/TSG.2016.2527821.
[15] J. Khalili, N.M. Dehkordi, M. Hamzeh, Distributed event-triggered secondary frequency control of islanded AC microgrids under cyber attacks with input time delay, Electr. Power Energy Syst. 143 (2022) 1–11.
[16] M. Iqbal, J. Laurent, A. Benmouna, M. Becherif, H.S. Ramadan, F. Claude, Ageing-aware load following control for composite-cost optimal energy management of fuel cell hybrid electric vehicle, Energy 254 (A) (2022) 1–15.
[17] R.R. Shukla, M.M. Garg, A.K. Panda, D. Das, Enhancing load frequency control with plug-in electric vehicle integration in non-reheat thermal power systems, Electr. Eng. 106 (2024) 3305–3320.
[18] A.B. Kunya, Hierarchical bi-level load frequency control for multi-area interconnected power systems, Electr. Power Energy Syst. 155 (2024) 109600.
[19] M.U. Jan, A. Xin, M.A. Abdelbaky, H.U. Rehman, S. Iqbal, Adaptive and fuzzy PI controllers design for frequency regulation of isolated microgrid integrated with electric vehicles, IEEe Access. 8 (2020) no. 10.1109/ACCESS.2020.2993178.
[20] F.M. Gonzalez-Longatt, Impact of emulated inertia from wind power on under-frequency protection schemes of future power systems, J. Mod. Power Syst. Clean Energy 4 (2) (2018) 211–218.
[21] N. Taghizadegan, F. Babaei, A. Safari, A linear active disturbance rejection control technique for frequency control of networked microgrids, Energy Syst. 15 (2024) 807–826.
[22] S. Das, S. Panda, An optimized fractional order cascade controller for frequency regulation of power system with renewable energies and electric vehicles, Energy Syst. 14 (2023) 171–195, https://doi.org/10.1007/s12667-021-00461-9.
[23] D.K. Gupta, G. Dei, A.K. Soni, A.V. Jha, B. Appasani, N. Bizon, A. Srinivasulu, P. Nsengiyumva, Fractional order PID controller for load frequency control in a deregulated hybrid power system using aquila optimization, Results Eng. 23 (2024) 102442.
[24] B. Tek, Ş. Sönmez, S. Ayasun, Delay-dependent stability analysis of a two-area load frequency control system including electric vehicle aggregator and dynamic demand response, in: Proceedings of the 12th Int'l Conference on Electrical and Electronics Engineering, Bursa, Turkey, 2020.
[25] W. Tian, J. He, L. Niu, W. Zhang, X. Wang, Z. Bo, Load frequency control in renewable based micro grid with deep neural network based controller, Results Eng. 25 (2025) 103554.
[26] J. Ullmark, L. Göransson, F. Johnsson, Frequency reserves and inertia in the transition to future electricity systems, Energy Syst. 14 (2023), https://doi.org/10.1007/s12667-023-00568-1.

[27] N. Saikia, N.K. Das, Load frequency control of a two area multi-source power system with electric vehicle, J. Control Autom. Electr. Syst. 34 (2023) 394–406.

[28] A.B. Kunya, M. Argin, Y. Jibril, Y.A. Shaaban, Improved model predictive load frequency control of interconnected power system with synchronized automatic generation control loops, Beni Suef Univ. J. Basic Appl. Sci. 9 (47) (2020) 1–13, https://doi.org/10.1186/s43088-020-00072-w.

[29] A.B. Kunya, M. Argin, Model predictive load frequency control of multi area interconnected power system, in: Proceedings of the IEEE Texas Power and Energy Conference, College Station, TX, USA, 2018.

[30] A. Garcés-Ruiz, W. Gil-González, O.D. Montoya, Stability analysis for an ad-hoc model predictive control in DC/DC converters with a constant power load, Results Eng. 22 (2024) 102262.

[31] T.H. Mohamed, Load frequency control of an isolated small power system with contribution of vehicle-to-grid V2G scheme, in: Proceedings of the 2016 Eighteenth International Middle East Power Systems Conference (MEPCON), Cairo, Egypt, 2016.

[32] S. Mishra, P.C. Nayak, U.C. Prusty, R.C. Prusty, Model predictive controller based load frequency control of isolated microgrid system integrated to plugged-in electric vehicle, in: Proceedings of the 1st Odisha International Conference on Electrical Power Engineering, Communication and Computing Technology (ODICON), Bhubaneswar, India, 2021, https://doi.org/10.1109/ODICON50556.2021.9428956.

[33] A. Oshnoei, M. Kheradmandi, S.M. Muyeen, N.D. Hatziargyriou, Disturbance observer and tube-based model predictive controlled electric vehicles for frequency regulation of an isolated power grid, IEEe Trans. Smart Grid 12 (5) (2021) 4351–4362.

[34] J. Pan, S. Yu, M. Ma, Model predictive load frequency control of isolated micro-grid with electrical vehicles, in: Proceedings of the 37th Chinese Control Conference (CCC), Wuhan, China, 2018.

[35] A. Ali, B. Khan, C.A. Mehmood, Z. Ullah, S.M. Ali, R. Ullah, Decentralized MPC based frequency control for smart grid, in: Proceedings of the International Conference on Energy Conservation and Efficiency (ICECE), Lahore, Pakistan, 2017, https://doi.org/10.1109/ECE.2017.8248819.

[36] S. Cai, R. Matsuhashi, Model predictive control for EV aggregators participating in system frequency regulation market, IEEe Access. 9 (2021) 80763–80771, no. 10.1109/ACCESS.2021.3085345.

[37] G. Zhang, Y. Ge, Z. Ye, M. Al-Bahrani, Multi-objective planning of energy hub on economic aspects and resources with heat and power sources, energizable, electric vehicle and hydrogen storage system due to uncertainties and demand response, J. Energy Storage 57 (2023) 1–14.

[38] P. Li, W. Hu, X. Xu, Q. Huang, Z. Liu, Z. Chen, A frequency control strategy of electric vehicles in microgrid using virtual synchronous generator control, Energy 189 (2019) 116389.

[39] A. Tanikawa, Analysis of the riccati equation of the optimal filter with disturbance decoupling property for linear stochastic systems, Int. J. Innov. Comput. Inf. Control 15 (3) (2019) 811–824.

[40] F.H. Jufri, J.J.B. Sudiarto, I. Garniwa, Development of virtual inertia control with state-of-charge recovery strategy using coordinated secondary frequency control for optimized battery capacity in isolated low inertia grid, Energies 16 (2023) 5463. . (Basel).